

Weyl points of mechanical diamond

Yuta Takahashi¹, Toshikaze Kariyado², and Yasuhiro Hatsugai³

¹*Graduate School of Pure and Applied Science, University of Tsukuba, Tsukuba, Ibaraki 305-8571, Japan*

²*International Center for Materials Nanoarchitectonics(WPI-MANA),*

National Institute for Materials Science, Tsukuba, Ibaraki 305-0044, Japan

³*Division of Physics, University of Tsukuba, Tsukuba, Ibaraki 305-8571, Japan*

(Dated: December 14, 2024)

A spring-mass model arranged in a diamond structure—mechanical diamond—is analyzed in terms of topology in detail. We find that, additional springs connecting the next-nearest-neighbor pairs of mass points and the modulation of the mass parameters to the pristine mechanical diamond generates several pairs of Weyl points in the frequency dispersion. Evolution of the Weyl point mapping in the Brillouin zone against uniform outward tension is shown and explained from the view point of the point group symmetry, especially tetrahedral symmetry of the NNN springs. Interestingly, there happens a rapid transmutation of the monopole charges of the Weyl points as the tension changes. We also show Fermi arcs as surface modes in the case that anisotropy is introduced in the model.

I. INTRODUCTION

Topological semimetals, which are characterized by isolated gapless points or lines in their band structure, have been intensively studied both in theoretical and experimental view points recently. There are two classes of topological semimetals: one requires some symmetry for protection of the gapless points, while the other is purely topological. The former includes Dirac semimetals with time reversal and spatial inversion symmetries, or nodal line semimetals that are protected by reflection symmetry, for instance¹⁻⁷. On the other hand, the latter includes Weyl semimetals where either of time reversal or spatial inversion symmetry should be broken⁸⁻¹³. Namely, for the Weyl semimetals, symmetry breaking is the key for generating gapless points (Weyl points). The Weyl points are created/annihilated as pairs and each of a pair carries ± 1 topological charge, and the conservation of the topological (or monopole) charge is behind the stability of the Weyl points. In relation to topology, surface states of Weyl semimetals are notable: a Weyl semimetal is characterized by a Fermi arc, which is an isoenergy line of the surface state at the Fermi energy connecting a pair of Weyl points projected onto the surface Brillouin zone^{14,15}. We can relate the surface state (and Fermi arc) with the bulk Chern number, forming a typical example of bulk-edge correspondence¹⁶.

Currently, the concept of “topological insulators” and bulk-edge correspondence is extended to wider and wider variety of systems including classical systems such as photonic crystals^{17,18} and mechanical systems¹⁹⁻²⁵. It is possible to mimic quantum Hall states, quantum spin Hall states, and other topologically nontrivial states by appropriate artificial designs. This artificial nature is an advantage of the classical topological systems over the quantum electronic systems. Namely, the classical systems usually have better controllability than the quantum ones, and enables us to access parameter regions that are impossible or difficult in quantum systems. Mechanical graphene, a spring-mass model with the honeycomb

structure having Dirac cones in its frequency dispersion, enjoys this controllable feature²⁶⁻²⁸. For instance, the number and positions of the Dirac cones can be changed simply by a uniform outward tension. If the Dirac cones are gapped out by a time-reversal symmetry breaking term, there appear chiral edge mode, and the same uniform tension causes a flip in the flowing direction of the chiral edge mode. Mechanical graphene has a natural extension in three-dimension, i.e., mechanical diamond that is a spring-mass model with diamond structure²⁹. We have found that mechanical diamond is a classical counterpart of the nodal line semimetal, and a (modified) chiral symmetry is the key for line node protection²⁹.

In this paper, we investigate symmetry breaking effects in mechanical diamond. The (modified) chiral symmetry is broken by introducing springs connecting next-nearest-neighbor (NNN) pairs of mass points in addition to the original ones for the nearest neighbor (NN) pairs, and introducing modulation in mass of the mass points. This symmetry breaking eliminates the line nodes and generates several Weyl points. It is noticed that the tetrahedral symmetry of the system after introducing NNN springs is crucial in determining the number of the Weyl points. As in the case of mechanical graphene, the uniform outward tension induces movement of the Weyl points along the line originally being line nodes. Interestingly, an exchange of chirality (or topological charge) occurs as the Weyl nodes travel about. We also investigate surface states to see Fermi arcs associated with the nontrivial topology in the bulk with Weyl points. In the following, we start with describing two types of the mechanical diamond, a NN model and a NNN model in Sec. II. Section III is for numerical methods to identify Weyl points. Mappings of the Weyl points for an isotropic case and an anisotropic case are shown in Sec. IV, and the results are interpreted in terms of symmetry. Section V considers Fermi arcs for the anisotropic case in a system with a boundary. The paper is concluded in Sec. VI.

II. MODEL

A. Nearest-neighbor (NN) model

A mechanical diamond is a classical model composed of mass points and springs arranged in a diamond structure. We first consider NN model, where the springs connect the neighboring pairs of the mass points. The parameters describing our model are spring constant of the NN springs κ , mass of the mass points m , natural length of the NN springs l_0 and distance between the neighboring mass points R_0 . If we apply uniform outward tension, the distance R_0 can be larger than the natural length l_0 . This deformation is enabled by a proper boundary condition. For simplicity, m is set to unity in this NN model. The dynamical variables of the model are $\mathbf{x}_{\mathbf{R}a} = (x_{\mathbf{R}a}, y_{\mathbf{R}a}, z_{\mathbf{R}a})$, which are displacements of mass points from the equilibrium positions with \mathbf{R} denoting the lattice points and a being a sublattice index. In the following, we focus on infinitesimal oscillation about the equilibrium positions, and $\mathbf{x}_{\mathbf{R}a}$ is regarded as a small quantity.

The elastic energy of a single linear spring U_s is approximated as $U_s \simeq U_0 + U_1(\delta x_\lambda) + U_2(\delta x_\mu \delta x_\nu)$, with $\delta \mathbf{x}$ indicating a difference between the displacements of the neighboring pair of the mass points. The U_1 -term that is first order in δx_λ can be finite for a single spring, but if we consider all the springs connected to a single mass point, the terms cancel out with each other. Then, the dynamics of the system is governed by the U_2 -term that is second order in δx_λ . The U_2 -term is explicitly written as

$$U_2(\delta x_\mu \delta x_\nu) = \frac{1}{2} \kappa \delta x_\mu \gamma_{\mathbf{R}_0}^{\mu\nu} \delta x_\nu, \quad (1)$$

where $\gamma_{\mathbf{R}_0}^{\mu\nu} = (1 - \eta)\delta^{\mu\nu} + \eta \hat{R}_0^\mu \hat{R}_0^\nu$, $\hat{\mathbf{R}}_0 = \mathbf{R}_0/|\mathbf{R}_0|$ and $\eta \equiv l_0/R_0$. The summation over μ and ν , which run through three spatial directions (x, y, z), is implicitly taken. Importantly, the tension parameter η determines the U_2 -term.

Substituting four NN vectors $\mathbf{R}_0^{(i)}$ ($i = 1, 2, 3, 4$) into $U_2(\delta x_\mu \delta x_\nu)$, and applying Fourier transformation in time and space, i.e., using $\mathbf{x}_{\mathbf{R}a} = \frac{1}{N} \sum_{\mathbf{k}} e^{i(\mathbf{k} \cdot \mathbf{R} + \omega t)} \phi_{\mathbf{k}a}$, the

Newton's equation of motion becomes

$$\hat{\Gamma}(\mathbf{k})\phi(\mathbf{k}) = \omega^2\phi(\mathbf{k}), \quad (2)$$

where

$$\hat{\Gamma}(\mathbf{k}) = 4\kappa(1 - \frac{2}{3}\eta)\hat{1} + \begin{pmatrix} \hat{0} & \hat{\Gamma}_{AB}(\mathbf{k}) \\ \hat{\Gamma}_{AB}^\dagger(\mathbf{k}) & \hat{0} \end{pmatrix}, \quad (3)$$

and $\hat{\Gamma}_{AB}(\mathbf{k}) = -\kappa(\hat{\gamma}_4 + e^{-i\mathbf{k} \cdot \mathbf{a}_1}\hat{\gamma}_1 + e^{-i\mathbf{k} \cdot \mathbf{a}_2}\hat{\gamma}_2 + e^{-i\mathbf{k} \cdot \mathbf{a}_3}\hat{\gamma}_3)$, with $\hat{\gamma}_i \equiv \hat{\gamma}_{\mathbf{R}_0^{(i)}}$ ($i = 1, 2, 3, 4$). A frequency dispersion is obtained from this secular equation. Note that $\hat{\Gamma}(\mathbf{k})$ has a chiral symmetry if the diagonal terms are subtracted, i.e., $\hat{\Gamma}'(\mathbf{k}) = \hat{\Gamma}(\mathbf{k}) - 4\kappa(1 - \frac{2}{3}\eta)$ anticommutes with $\hat{\Upsilon} = \text{diag}(1, 1, 1, -1, -1, -1)$. As discussed in Ref. 29, by making use of the Berry's parameterization of a two band effective model near a gap closing point, it can be shown that the gap closing point should form a line (line node) in the 3D Brillouin zone³⁰ with the chiral symmetry. In contrast, the gap closing point becomes an isolated point (Weyl point) in the 3D Brillouin zone without chiral symmetry. In the following, we consider to add a term breaking the chiral symmetry in mechanical diamond.

B. Next-nearest-neighbor (NNN) model

In order to break the chiral symmetry, we introduce (i) springs connecting the next-nearest-neighbor pairs of the mass points on one of the sublattices only (say, the sublattice A out of the sublattices A and B) (see Fig. 1), and (ii) difference in the mass of the mass points between the two sublattices. Following the arguments in the previous subsection, and using six NNN vectors $\mathbf{R}_1^{(i)}$ ($i = 1, 2, \dots, 6$) in Fig. 1, the secular equation to be solved becomes

$$\hat{\Gamma}_{NNN}(\mathbf{k})\phi'(\mathbf{k}) = \omega^2\phi'(\mathbf{k}), \quad (4)$$

with

$$\hat{\Gamma}_{NNN}(\mathbf{k}) = \begin{pmatrix} \hat{\Gamma}_{AA}(\mathbf{k})/m & \hat{\Gamma}_{AB}(\mathbf{k})/\sqrt{m} \\ \hat{\Gamma}_{AB}^\dagger(\mathbf{k})/\sqrt{m} & \hat{\Gamma}_{BB} \end{pmatrix}. \quad (5)$$

Here,

$$\hat{\Gamma}_{AA}(\mathbf{k}) = \hat{\Gamma}_{BB} + 2\kappa'_1[1 - \cos(\mathbf{k} \cdot \mathbf{a}_1)]\hat{\gamma}'_1 + 2\kappa'_2[1 - \cos(\mathbf{k} \cdot \mathbf{a}_2)]\hat{\gamma}'_2 + 2\kappa'_3[1 - \cos(\mathbf{k} \cdot \mathbf{a}_3)]\hat{\gamma}'_3 + 2\kappa'_4[1 - \cos(\mathbf{k} \cdot (\mathbf{a}_1 - \mathbf{a}_2))]\hat{\gamma}'_4 + 2\kappa'_5[1 - \cos(\mathbf{k} \cdot (\mathbf{a}_2 - \mathbf{a}_3))]\hat{\gamma}'_5 + 2\kappa'_6[1 - \cos(\mathbf{k} \cdot (\mathbf{a}_3 - \mathbf{a}_1))]\hat{\gamma}'_6, \quad (6)$$

with $\hat{\gamma}'_i \equiv \hat{\gamma}_{\mathbf{R}_1^{(i)}} = (1 - \eta')\delta^{\mu\nu} + \eta' \hat{R}_1^{(i)\mu} \hat{R}_1^{(i)\nu}$, $\hat{\mathbf{R}}_1 = \mathbf{R}_1/|\mathbf{R}_1|$, $\hat{\Gamma}_{BB} = 4\kappa(1 - \frac{2}{3}\eta)\hat{1}$ and $\hat{\Gamma}_{AB}(\mathbf{k})$ is unchanged from the previous subsection. The new tension parameter η' is defined as $\eta' \equiv l_1/R_1$ where l_1 is natural length of

the NNN springs and $R_1 = |\mathbf{R}_1|$. A uniform and isotropic outward tension preserves the ratio between R_0 and R_1 , and therefore, we have $\eta' = \frac{\eta'_0}{\eta_0}\eta$ where η_0 and η'_0 are the tension parameters of the NN and NNN springs at some

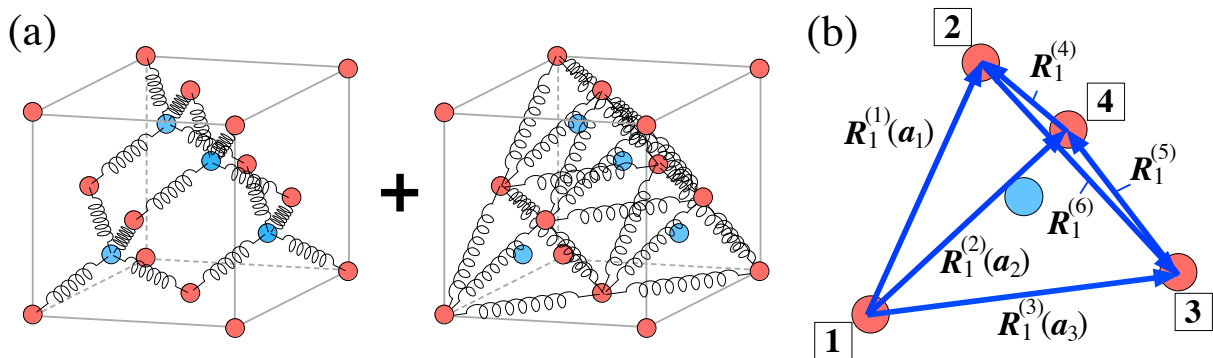


FIG. 1. (a) Schematic picture of the NNN model. Red (blue) mass points are labeled as sublattice A (B). (b) Definitions of NNN vectors $\mathbf{R}_1^{(i)}$. In particular, the three vectors $\mathbf{R}_1^{(1)}$ - $\mathbf{R}_1^{(3)}$ are exactly the same as the unit translation vectors \mathbf{a}_1 - \mathbf{a}_3 respectively. The four vertices of a tetrahedron formed by the NNN springs are numbered (from 1 to 4) to discuss a symmetry in §IV.

reference tension, respectively.

Note that we have assigned different spring constants for NNN springs lying in different directions, i.e., κ'_i ($i = 1, 2, \dots, 6$) for the NNN springs in the $\mathbf{R}_1^{(i)}$ directions. For the NN springs, the forces exerted on a single mass point are balanced between four springs in equilibrium, and it is better to assign the same spring constants for four springs to keep the ideal diamond structure. On the other hand, for the NNN springs, the forces on a mass point are balanced in a pairwise way in each of the six directions along $\mathbf{R}_1^{(i)}$ in equilibrium, and the ideal diamond structure is kept even if we assign different spring constants for different directions. For the mass parameters, we use m for sublattice A and 1 for sublattice B. Naively, the variation of mass makes the problem a generalized eigenvalue problem, but for convenience, we have reformulated it into a standard eigenvalue problem with an hermitian matrix $\hat{\Gamma}_{NNN}(\mathbf{k})$ by absorbing the factor m into the eigenvectors as $\phi'(\mathbf{k}) = \text{diag}(\sqrt{m}, \sqrt{m}, \sqrt{m}, 1, 1, 1)\phi(\mathbf{k})$. When we have discussed the chiral symmetry in NN model, subtraction of the diagonal part proportional to an identity matrix was essential. For NNN model, since the block matrix $\hat{\Gamma}_{AA}$ depends on the momentum, we cannot remove it as the NN model.

III. NUMERICAL METHOD

Our major task in the following is to identify Weyl points. In numerics, it is nontrivial to distinguish a strictly gapless point from a tiny but finitely gapped point if we only look at eigenvalue spectra. Therefore, we try to extract more information from eigenstates. Specifically, we numerically locate monopoles in Brillouin zone (Weyl points) by evaluating Berry curvature by adapting the method for the Chern number calculation^{31,32}. The procedure is as follows [see also Fig. 2(a)]. First, the Brillouin zone is divided into coarse cubes whose corners

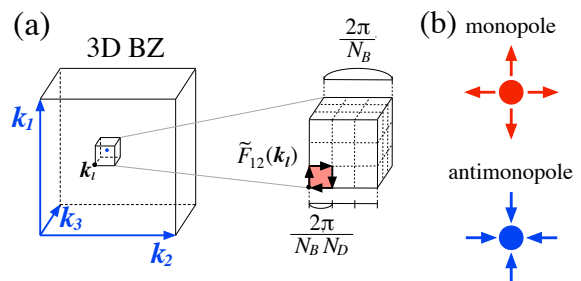


FIG. 2. (a) Schematic picture of the procedure to detect Weyl points. A lattice field strength $\tilde{F}_{12}(\mathbf{k}_l)$ is calculated on the red area as a part of one face of a minicube. (b) Definition of a monopole (antimonopole). The monopole (antimonopole) corresponds to chirality + (-). The Berry flux flows in the direction of arrows.

are labeled by $\mathbf{k}_l = (k_{l_1}, k_{l_2}, k_{l_3})$ where $\mathbf{l} = (l_1, l_2, l_3)$, $k_{l_\mu} = 2\pi l_\mu / N_B$ and $l_\mu = 0, \dots, N_B - 1$. Then we define a $U(1)$ link variable by

$$U_\mu(\mathbf{k}) \equiv \frac{\det \psi^\dagger(\mathbf{k}) \psi(\mathbf{k} + \hat{\mathbf{e}}_\mu)}{|\det \psi^\dagger(\mathbf{k}) \psi(\mathbf{k} + \hat{\mathbf{e}}_\mu)|}, \quad (7)$$

where $\psi(\mathbf{k})$ is a triplet state of which components are three states with lower frequencies. We have also put in a shorthand notation $\hat{\mathbf{e}}_\mu = 2\pi/(N_B N_D)(\delta_{1\mu}, \delta_{2\mu}, \delta_{3\mu})$ with a quantity N_D denoting the number of discretized mesh points on the surface of the coarse cube. For the square spanned by \mathbf{k}_l , $\mathbf{k}_l + \hat{\mathbf{e}}_\mu$, $\mathbf{k}_l + \hat{\mathbf{e}}_\nu$ and $\mathbf{k}_l + \hat{\mathbf{e}}_\mu + \hat{\mathbf{e}}_\nu$ ($\mu \neq \nu$), a lattice field strength is given as

$$\tilde{F}_{\mu\nu}(\mathbf{k}_l) \equiv \text{Arg} \frac{U_\mu(\mathbf{k}_l) U_\nu(\mathbf{k}_l + \hat{\mathbf{e}}_\mu)}{U_\mu(\mathbf{k}_l + \hat{\mathbf{e}}_\nu) U_\nu(\mathbf{k}_l)}, \quad (8)$$

$$-\pi < \tilde{F}_{\mu\nu}(\mathbf{k}_l) \leq \pi,$$

and a monopole charge of one coarse cube \tilde{C}_l is computed from $\tilde{F}_{\mu\nu}(\mathbf{k}_l)$ as

$$\begin{aligned} \tilde{C}_l = \frac{1}{2\pi} \sum_{i,j=0}^{N_D-1} & [-\tilde{F}_{12}(\mathbf{k}_l + i\hat{e}_1 + j\hat{e}_2) - \tilde{F}_{23}(\mathbf{k}_l + i\hat{e}_2 + j\hat{e}_3) - \tilde{F}_{31}(\mathbf{k}_l + i\hat{e}_3 + j\hat{e}_1) \\ & + \tilde{F}_{12}(\mathbf{k}_{l+(0,0,1)} + i\hat{e}_1 + j\hat{e}_2) + \tilde{F}_{23}(\mathbf{k}_{l+(1,0,0)} + i\hat{e}_2 + j\hat{e}_3) + \tilde{F}_{31}(\mathbf{k}_{l+(0,1,0)} + i\hat{e}_3 + j\hat{e}_1)]. \end{aligned} \quad (9)$$

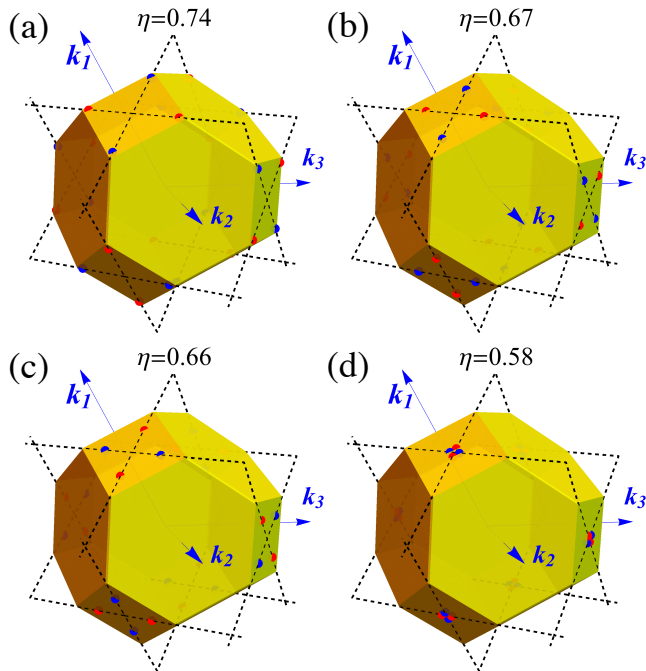


FIG. 3. Weyl points for the isotropic case. The tension parameters are (a) $\eta = 0.74$, (b) $\eta = 0.67$, (c) $\eta = 0.66$ and (d) $\eta = 0.58$. The three blue arrows marked with \mathbf{k}_1 , \mathbf{k}_2 and \mathbf{k}_3 are the reciprocal vectors of the diamond lattice. The dashed lines indicate the line nodes in the chiral symmetric case, which are found irrespective of the value of η . (For the chiral symmetric case, there are other line nodes in a certain range of η . See Fig. 4 and Ref. 29.)

When this monopole charge results in a nonzero integer, at least one Weyl point exists in that cube. (In general, we have to note that even if this monopole charge is zero, we still have a chance to find multiple Weyl points with compensated charges.) Hence, we pick up cubes with finite monopole charges and repeat this procedure (subdivide into smaller cubes) until we have a solo Weyl point in each cube.

IV. POSITION OF WEYL POINTS

A. Isotropic case

Equipped with the method in the previous section, we investigate Weyl points in NNN model of mechanical diamond. Figure 3 shows Weyl points for an isotropic case, where $\kappa = 1/(1 - \frac{2}{3}\eta)$, $\kappa'_i = 0.2/(1 - \frac{2}{3}\eta)$ ($i = 1, 2, \dots, 6$),

$\eta_0 = 1$, $\eta'_0 = 0.8$ and $m = 2$. We have applied the dividing procedure twice. In the first step, we use $N_B^{1st} = 41$ and $N_D^{1st} = 5$, and in the second step, we use $N_B^{2nd} = 5$ and $N_D^{2nd} = 3$, in which the length of the edge of the smallest cube is $1/205$ of the Brillouin zone size. A red (blue) point stands for a Weyl point of a monopole (antimonopole) as described in Fig. 2(b). We find six pairs of the Weyl points moving from the W points to the X points as the tension increases, or η decreases. Note that the line node in NN model passes through the line connecting the W and X points. In decreasing η , the Weyl points are created as pairs at the W points, and annihilated with those from the other pairs at the X points.

Remarkably, the colors of the Weyl points are different between Fig. 3(b) and Fig. 3(c), i.e., there is a rapid transmutation of the monopole charge from positive to negative (or vice versa). This transmutation occurs in between $\eta = 0.67$ and $\eta = 0.66$. Figure 4 illustrates the detailed process of the transmutation. Because of the three-fold rotational symmetry and the reflection symmetry of the system, it is sufficient to examine one of the square faces of the fcc Brillouin zone. For an illustrative purpose, we put numbers on found Weyl points as in the right panels of Fig. 4. Also as a guidance, we draw line nodes for the corresponding NN model with chiral symmetry in Fig. 4. (There are no line nodes anymore without the chiral symmetry.) As η decreases from 0.6680 to 0.6635, the number of the Weyl points on the square face changes as $4 \rightarrow 12 \rightarrow 4$. For $\eta = 0.6680$, the four Weyl points (No. 1–No. 4) are at the crossing points between the straight and circularlike line nodes. For $\eta = 0.6675$, new eight Weyl points (No. 5–No. 8 and No. 5'–No. 8') are found on the circularlike line node. These new Weyl points are created as pairs of No. 5–No. 6, No. 6'–No. 7', No. 7–No. 8, and No. 8'–No. 5'. For $\eta = 0.6645$, the two pairs of the monopoles No. 5–No. 5' and No. 7–No. 7' approach to the antimonopoles No. 1 and No. 3 along the trace of the circularlike line nodes, respectively. At the same time, the two pairs of the antimonopoles No. 6–No. 6' and No. 8–No. 8' come close to the monopoles No. 2 and No. 4. Finally, only two monopoles and two antimonopoles that have the opposite charges from the $\eta = 0.6680$ case remain at the intersection of the straight and circularlike line nodes for $\eta = 0.6635$.

It is helpful to think of the tetrahedral symmetry of the NNN springs in understanding the number of the Weyl points in the first Brillouin zone. Here, we use the numbers in Fig. 1(b). There are $4! = 24$ symmetric operations to exchange the vertices in the tetrahedron. This operation is mapped to be a permutation of $(1, 2, 3, 4)$. When a Weyl point is generated at a generic point, this

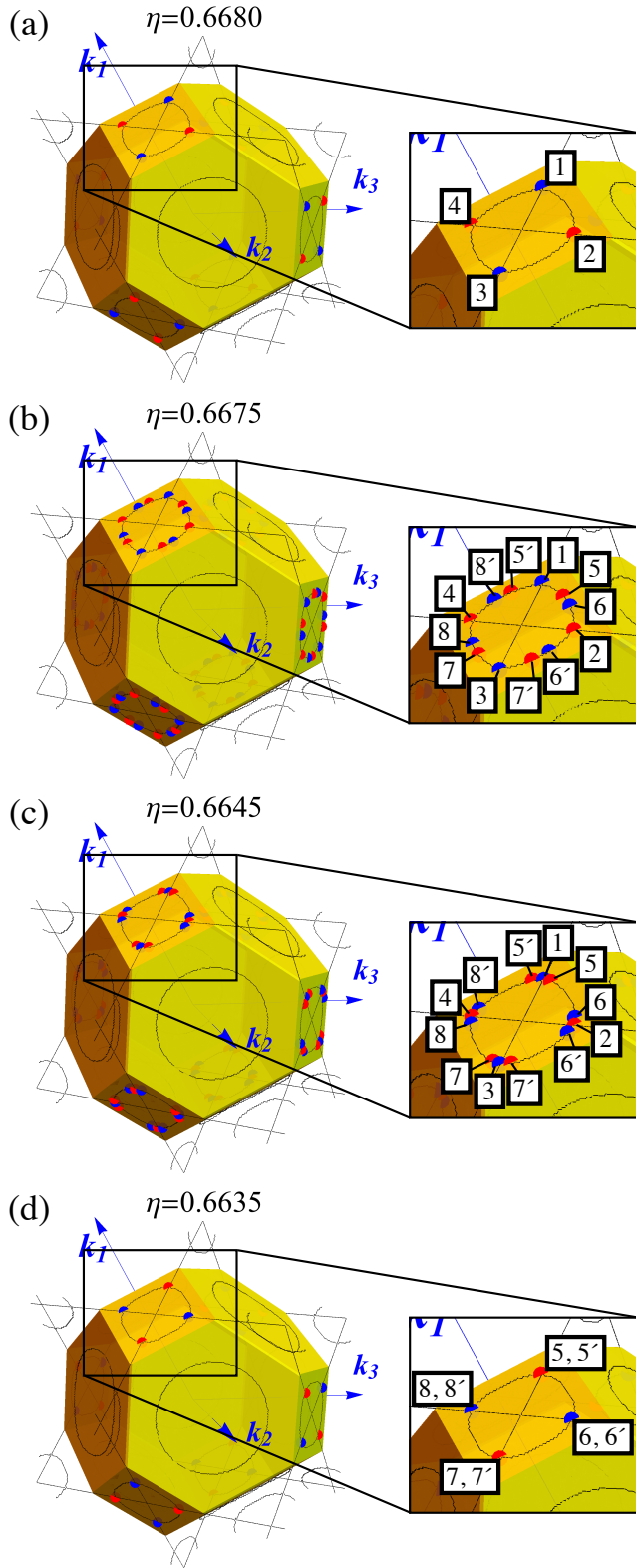


FIG. 4. Details for the switch of the positive and negative chiralities. The tension parameters are (a) $\eta = 0.6680$, (b) $\eta = 0.6675$, (c) $\eta = 0.6645$ and (d) $\eta = 0.6635$. Black lines represent the numerically obtained line nodes in the NN model (i.e., with chiral symmetry) for each η .

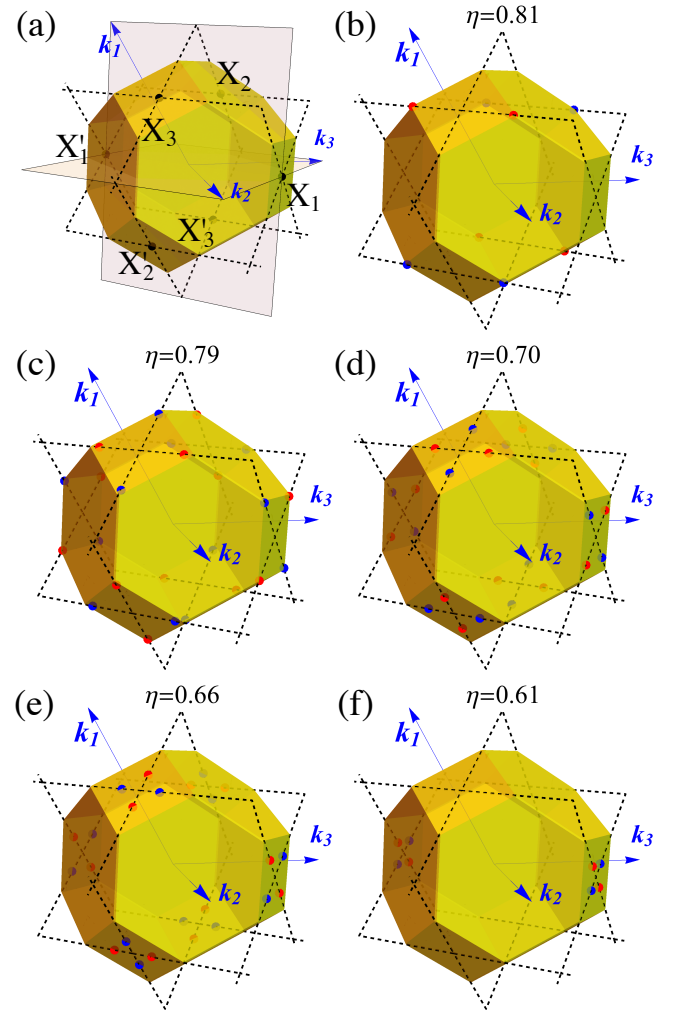


FIG. 5. (a) Notations for the high symmetric points in the Brillouin zone. X_i and X'_i ($i = 1, 2, 3$) points are equivalent respectively. The two planes indicate mirror planes in the Brillouin zone remaining in the anisotropic case. (b)-(f) Weyl points for the anisotropic case. The tension parameters are (b) $\eta = 0.81$, (c) $\eta = 0.79$, (d) $\eta = 0.70$, (e) $\eta = 0.66$ and (f) $\eta = 0.61$.

point transfers to 24 points by the permutation, in which 12 points are moved by the even permutation while the other 12 points by the odd permutation. The chirality of the Weyl points actually depends on whether the permutation is even or odd. In contrast, a Weyl point on the high symmetric X-W lines relocate to 12 (instead of 24) points by the permutation. Note that the mapping of Weyl points by the permutation is consistent with the time reversal symmetry in NNN model.

B. Anisotropic case

In the previous paragraph, we have seen that the number of the Weyl points are restricted by the tetrahedral

symmetry. Here, let us introduce anisotropy to break this symmetry. In the isotropic case discussed so far, we have been using $\eta'/\eta = 0.8$ for all the NNN springs. In order to induce anisotropy, we modify η'/η for the springs along $\mathbf{R}_1^{(1)}$ direction to 1. The system does not have tetrahedral symmetry anymore, but again, it should be noted that the forces on a single mass point cancel out in a pairwise manner in equilibrium, and therefore, the applied modification is not harmful in keeping the ideal diamond structure. Figure 5 shows Weyl points for the anisotropic case. Due to the symmetry breaking, timing of the creation and the annihilation differs from the isotropic case. As we decrease η , two pairs of Weyl points are generated in $k_1 = \pm\pi$ plane at $\eta = 0.81$. Then, other four pairs emerge at $\eta = 0.79$. (Remember that in the isotropic case, the six pairs are created simultaneously.) All six pairs switch the chirality in between $\eta = 0.70$ and $\eta = 0.66$, although the switch does not take place simultaneously. The switch of the four pairs near X_2, X'_2, X_3 and X'_3 points is first and that of the two pairs near X_1 and X'_1 points is second. Finally, only two pairs near the X_1 and X'_1 points remain for $\eta = 0.61$.

As we have seen, in the isotropic case, if a Weyl point is generated on X-W lines, the symmetry automatically gives 12 Weyl points in total. In the anisotropic case, the multiplicity of the Weyl points obeys a different rule. The tetrahedral symmetry is broken in the anisotropic model, but it still has two mirror plane leading to the exchange of $1 \leftrightarrow 2$ and $3 \leftrightarrow 4$ [see Fig. 1(b)]. For $\eta = 0.81$ [Fig. 5(b)], we see red points on the square face containing X_3 . Although there are two different mirror planes, both of them map a red point on this surface to the same blue point (note the periodicity of the Brillouin zone), and the multiplicity of the Weyl points caused by the mirror symmetry is 2. Then, even if we also consider the multiplicity by the time reversal symmetry, the total number of the Weyl points in the Brillouin zone is 4, which is less than 12. The key is that the square faces of the Brillouin zone boundary are no longer all the same in terms of the symmetry, and pair creation/annihilation on these faces can take place independently.

V. BULK SECTION CHERN NUMBER AND FERMI ARC

In this section, we show chiral edge states (or Fermi arc in this case) characterized by a bulk topological number. Let us start with the definition of the bulk topological number. In our 3D model, we have section Chern number (SCN)^{33–36}, whose definition is

$$C(k_i) = -\frac{i}{2\pi} \int_S \text{Tr} d\mathcal{A} \Big|_{k_i: \text{fixed}}. \quad (10)$$

Here, \mathcal{A} is a non-Abelian Berry connection $\mathcal{A} = \psi^\dagger d\psi$. The state ψ is a triplet formed by three eigenstates with lower frequencies. The integration is taken over the two-dimensional Brillouin zone with k_i ($i = 1, 2, 3$) fixed. In

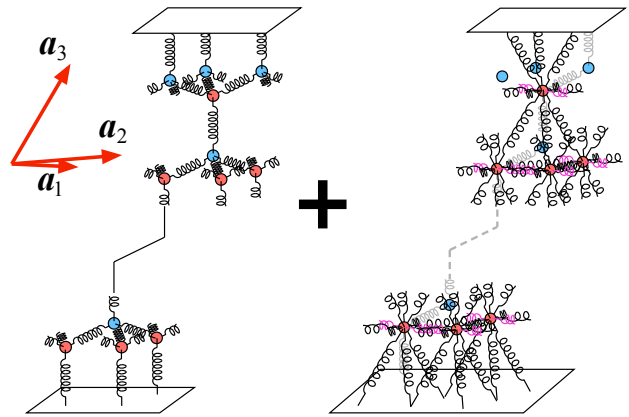


FIG. 6. Schematic picture of the NNN system with a boundary. The tension parameter for the magenta springs, which are arranged to be parallel to the surface, is different from the one for five other NNN springs.

the isotropic case, the SCN is always trivial for any fixed momentum because of mirror planes passing through the k_1 -, k_2 -, and k_3 -axes. In the anisotropic model, on the other hand, $C(k_2)$ and $C(k_3)$ can be nontrivial in a certain range of fixed momentum due to the absence of a mirror plane through the k_2 - and k_3 -axes.

To obtain surface states, we consider a system that is periodic in \mathbf{a}_1 and \mathbf{a}_2 direction but finite in \mathbf{a}_3 direction. In the \mathbf{a}_3 direction, the system is terminated with the fixed boundary condition as illustrated in Fig. 6. The surface states with this boundary condition for the NN model has been discussed in our previous paper²⁹. Now for the NNN model, Fig. 7 shows $C(k_2)$ and surface states of a system with 400 layers in z direction for $\eta = 0.61$. As expected, we see chiral edge states connecting the third and the fourth lowest bands for k_2 with finite $C(k_2)$. $C(k_2)$ changes when the plane of fixed k_2 crosses a gapless point with topological charge, i.e., Weyl point. One monopole (antimonopole) adds +1 (−1) to the SCN. We also notice that the number of the chiral edge states matches to the SCN including the directions. Note that flat bands that is already found in the NN model³⁷ remain even in the NNN model. The Fermi arc is shown in Fig. 7(i), which has no dependence on wave number in the \mathbf{k}_1 direction here.

VI. CONCLUSION

To summarize, we have investigated Weyl points of the mechanical diamond. By introducing the NNN springs and the variation in the mass parameter, several pairs of the Weyl points in the frequency dispersion appear in the Brillouin zone. The Weyl point positions are numerically obtained by calculating topological charges. As a function of the tension parameter, the configuration of the Weyl points in the Brillouin zone shows an inter-

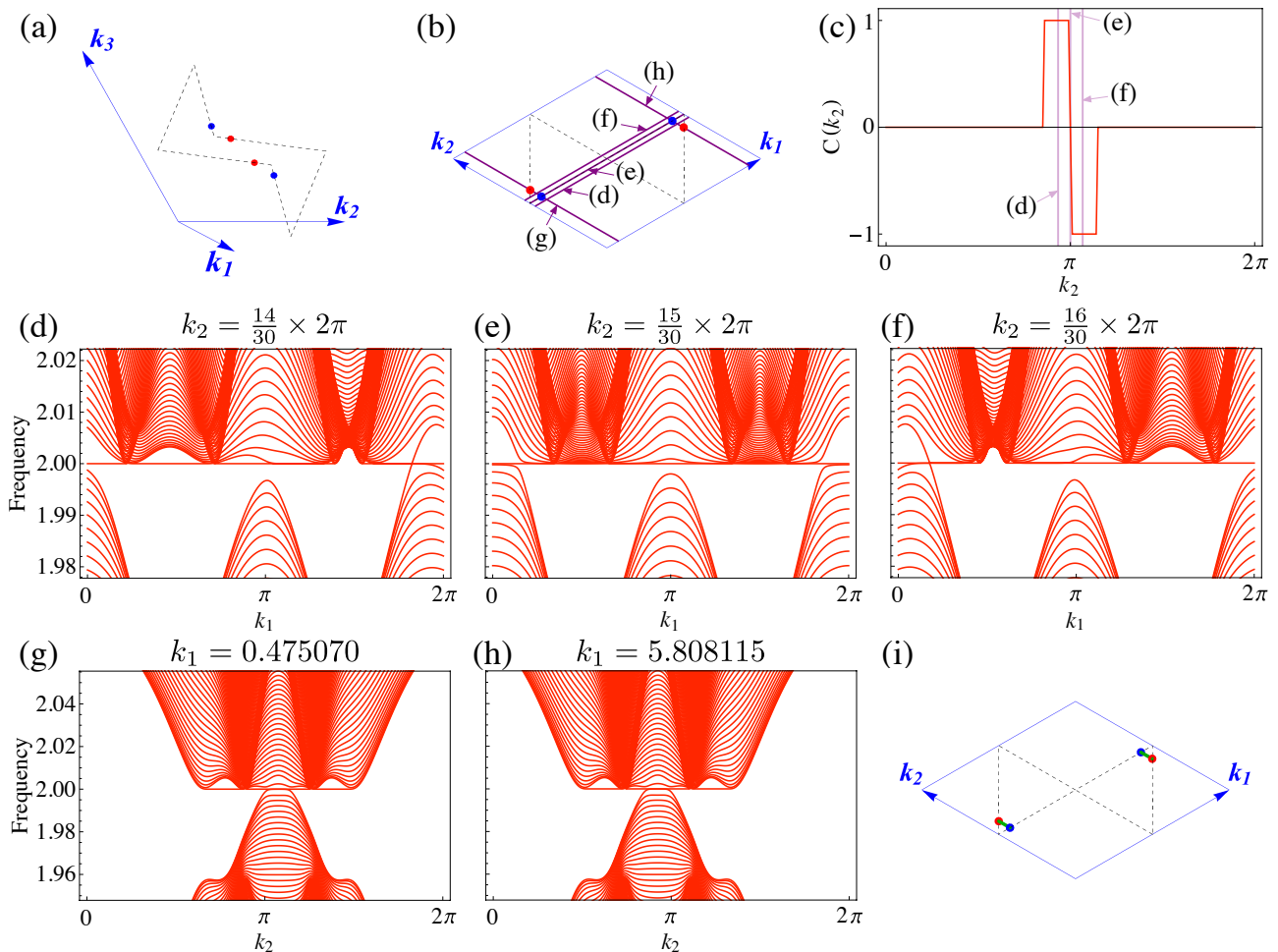


FIG. 7. (a) Weyl points of the anisotropic model for $\eta = 0.61$ in the parallelepiped Brillouin zone. (b) Weyl points projected onto the k_1 - k_2 plane. (c) SCN of this model in k_2 direction. (d)-(h) Surface band structures along the five purple lines named (d)-(h) in (b), respectively. In (d)-(f), k_2 is fixed to (d) $k_2 = \frac{14}{30} \times 2\pi$, (e) $k_2 = \frac{15}{30} \times 2\pi$ and (f) $k_2 = \frac{16}{30} \times 2\pi$, and the band structures are scanned by k_1 . In (g) and (h), k_1 is fixed to (g) $k_1 = 0.475070$ and (h) $k_1 = 5.808115$, and the band structures are scanned by k_2 . (The values of k_1 are numerically determined to hit the projected Weyl points.) (i) A Fermi arc projected onto the k_1 - k_2 plane, drawn as green lines.

esting evolution. For the isotropic case with tetrahedral symmetry, six pairs of the Weyl points move on the high-symmetric W-X lines as the tension increases. In a narrow range of the tension parameter, several extra pairs of Weyl points are created and annihilated, and after the annihilation, the chirality of the remaining Weyl points is flipped. For the anisotropic case without tetrahedral symmetry, the sequence of the creation/annihilation of Weyl points is a little different from the one in the isotropic case. Importantly, the broken tetrahedral sym-

metry allows finite SCN, and the relation between the surface states and the bulk SCN is explicitly demonstrated.

ACKNOWLEDGMENTS

We thank C. Mudry for useful discussions. This work was partly supported by JSPS KAKENHI Grant Numbers JP17K14358 (TK), JP16K13845 (YH), JP17H06138 and JP25107005 (YT, YH).

¹ S. M. Young, S. Zaheer, J. C. Y. Teo, C. L. Kane, E. J. Mele, and A. M. Rappe, Phys. Rev. Lett. **108**, 140405 (2012).

² Z. Wang, Y. Sun, X.-Q. Chen, C. Franchini, G. Xu, H. Weng, X. Dai, and Z. Fang, Phys. Rev. B **85**, 195320 (2012).

- ³ Z. K. Liu, B. Zhou, Y. Zhang, Z. J. Wang, H. M. Weng, D. Prabhakaran, S.-K. Mo, Z. X. Shen, Z. Fang, X. Dai, Z. Hussain, and Y. L. Chen, *Science* **343**, 864 (2014).
- ⁴ A. A. Burkov, M. D. Hook, and L. Balents, *Phys. Rev. B* **84**, 235126 (2011).
- ⁵ S. Kobayashi, Y. Yamakawa, A. Yamakage, T. Inohara, Y. Okamoto, and Y. Tanaka, *Phys. Rev. B* **95**, 245208 (2017).
- ⁶ Z. Yan, R. Bi, H. Shen, L. Lu, S.-C. Zhang, and Z. Wang, *Phys. Rev. B* **96**, 041103 (2017).
- ⁷ G. Bian, T.-R. Chang, R. Sankar, S.-Y. Xu, H. Zheng, T. Neupert, C.-K. Chiu, S.-M. Huang, G. Chang, I. Belopolski, D. S. Sanchez, M. Neupane, N. Alidoust, C. Liu, B. Wang, C.-C. Lee, H.-T. Jeng, C. Zhang, Z. Yuan, S. Jia, A. Bansil, F. Chou, H. Lin, and M. Z. Hasan, *Nat. Commun.* **7**, 10556 (2016).
- ⁸ S. Murakami, *New J. Phys.* **9**, 356 (2007).
- ⁹ A. A. Burkov and L. Balents, *Phys. Rev. Lett.* **107**, 127205 (2011).
- ¹⁰ C. Fang, M. J. Gilbert, X. Dai, and B. A. Bernevig, *Phys. Rev. Lett.* **108**, 266802 (2012).
- ¹¹ A. A. Soluyanov, D. Gresch, Z. Wang, Q. Wu, M. Troyer, X. Dai, and B. A. Bernevig, *Nature* **527**, 495 (2015).
- ¹² R. Okugawa and S. Murakami, *Phys. Rev. B* **96**, 115201 (2017).
- ¹³ L. Lu, Z. Wang, D. Ye, L. Ran, L. Fu, J. D. Joannopoulos, and M. Soljačić, *Science* **349**, 622 (2015).
- ¹⁴ X. Wan, A. M. Turner, A. Vishwanath, and S. Y. Savrasov, *Phys. Rev. B* **83**, 205101 (2011).
- ¹⁵ S.-Y. Xu, C. Liu, S. K. Kushwaha, R. Sankar, J. W. Krizan, I. Belopolski, M. Neupane, G. Bian, N. Alidoust, T.-R. Chang, H.-T. Jeng, C.-Y. Huang, W.-F. Tsai, H. Lin, P. P. Shibayev, F.-C. Chou, R. J. Cava, and M. Z. Hasan, *Science* **347**, 294 (2015).
- ¹⁶ Y. Hatsugai, *Phys. Rev. Lett.* **71**, 3697 (1993).
- ¹⁷ F. D. M. Haldane and S. Raghu, *Phys. Rev. Lett.* **100**, 013904 (2008).
- ¹⁸ Z. Wang, Y. D. Chong, J. D. Joannopoulos, and M. Soljačić, *Phys. Rev. Lett.* **100**, 013905 (2008).
- ¹⁹ E. Prodan and C. Prodan, *Phys. Rev. Lett.* **103**, 248101 (2009).
- ²⁰ C. L. Kane and T. C. Lubensky, *Nat. Phys.* **10**, 39 (2014).
- ²¹ H. C. Po, Y. Bahri, and A. Vishwanath, *Phys. Rev. B* **93**, 205158 (2016).
- ²² J. Paulose, B. G.-g. Chen, and V. Vitelli, *Nat. Phys.* **11**, 153 (2015).
- ²³ D. Z. Rocklin, B. G.-g. Chen, M. Falk, V. Vitelli, and T. C. Lubensky, *Phys. Rev. Lett.* **116**, 135503 (2016).
- ²⁴ P. Wang, L. Lu, and K. Bertoldi, *Phys. Rev. Lett.* **115**, 104302 (2015).
- ²⁵ J. E. S. Socolar, T. C. Lubensky, and C. L. Kane, *New J. Phys.* **19**, 025003 (2017).
- ²⁶ J. Cserti and G. Tichy, *Eur. J. Phys.* **25**, 723 (2004).
- ²⁷ Y.-T. Wang, P.-G. Luan, and S. Zhang, *New J. Phys.* **17**, 073031 (2015).
- ²⁸ T. Kariyado and Y. Hatsugai, *Sci. Rep.* **5**, 18107 (2015).
- ²⁹ Y. Takahashi, T. Kariyado, and Y. Hatsugai, *New J. Phys.* **19**, 035003 (2017).
- ³⁰ E. I. Blount, *Phys. Rev. B* **32**, 2935 (1985).
- ³¹ T. Fukui, Y. Hatsugai, and H. Suzuki, *J. Phys. Soc. Jpn.* **74**, 1674 (2005).
- ³² M. Hirayama, R. Okugawa, and S. Murakami, arXiv:1708.05791.
- ³³ J. E. Avron, R. Seiler, and B. Simon, *Phys. Rev. Lett.* **51**, 51 (1983).
- ³⁴ B. I. Halperin, *Jpn. J. Appl. Phys.* **26**, 1913 (1987).
- ³⁵ M. Kohmoto, B. I. Halperin, and Y.-S. Wu, *Phys. Rev. B* **45**, 13488 (1992).
- ³⁶ Y. Hatsugai, S. Ryu, and M. Kohmoto, *Phys. Rev. B* **70**, 054502 (2004).
- ³⁷ S. Ryu and Y. Hatsugai, *Phys. Rev. Lett.* **89**, 077002 (2002).